J Solid State Electrochem (2012) 16:1–8
DOI 10.1007/s10008-010-1263-x

ORIGINAL PAPER

The improvement of the high-rate charge/discharge performances of $LiFePO_4$ cathode material by Sn doping

Jun Ma · Baohua Li · Hongda Du · Chengjun Xu · Feiyu Kang

Received: 2 October 2010 / Revised: 24 November 2010 / Accepted: 28 November 2010 / Published online: 14 December 2010

Abstract Nanocrystalline $LiFePO_4$ and $LiFe_{0.97}Sn_{0.03}PO_4$ cathode materials were synthesized by an inorganic-based sol–gel route. The physicochemical properties of samples were characterized by X-ray diffraction, X-ray photoelectron spectroscopy, scanning electron microscopy, transmission electron microscopy, and elemental mapping. The doping effect of Sn on the electrochemical performance of $LiFePO_4$ cathode material was extensively investigated. The results showed that the doping of tin was beneficial to refine the particle size, increase the electrical conductivity, and facilitate the lithium-ion diffusion, which contributed to the improvement of the electrochemical properties of $LiFePO_4$, especially the high-rate charge/discharge performance. At the low discharge rate of 0.5 C, the $LiFe_{0.97}Sn_{0.03}PO_4$ sample delivered a specific capacity of 158 mAh g^{-1}, as compared with 147 mAh g^{-1} of the pristine $LiFePO_4$. At higher C-rate, the doping sample exhibited more excellent discharge performance. $LiFe_{0.97}Sn_{0.03}PO_4$ delivered specific capacity of 146 and 128 mAh g^{-1} at 5 C and 10 C, respectively, in comparison with 119 and 107 mAh g^{-1} for $LiFePO_4$. Moreover, the doping of Sn did not influence the cycle capability, even at 10 C.

Keywords Lithium iron phosphate · Sn doping · Cathode material · Sol–gel process

J. Ma · B. Li · H. Du · C. Xu · F. Kang
Advanced Materials Institute, Graduate School at Shenzhen, Tsinghua University,
Shenzhen, Guangdong Province 518055, China

J. Ma · F. Kang (✉)
Laboratory of Advanced Materials,
Department of Materials Science and Engineering, Tsinghua University,
Beijing 100084, China
e-mail: fykang@tsinghua.edu.cn

Introduction

Recently, lithium iron phosphate, as a promising cathode material for power lithium-ion batteries, has become a hot research topic because of its significant advantages, e.g., low cost, environmentally benign, excellent cycling stability, high theoretical capacity, and satisfactory thermal stability [1, 2]. However, due to its low intrinsic electrical conductivity (10^{-9} S cm^{-1}) [3] and the limited transport of lithium ion (10^{-14} cm^2 s^{-1}) [3], the theoretical capacity of $LiFePO_4$ is difficult to fully utilized at a useful rate, and thus, its large-scale applications are hindered greatly. Up to now, immense research activities have been concentrated on ameliorating these drawbacks. These efforts mainly involve coating $LiFePO_4$ particles with conductive agents [4–7] and doping the host framework with alien ions at the Li-site (M1 site) or/and Fe-site (M2 site) [8–15]. The former approaches could effectively improve the intergranular electrical conductivity. However, its contribution to enhancement of the rate capacity is limited, especially at high C-rate. The latter could effectively induce lattice relaxation, and as a result, the chemical diffusion of lithium ion in the crystal interior would be facilitated. However, doping in the host body without conductive agent coating is not enough to play its paramount role in improving the rate capability and the charge/discharge performance. Thus, researchers usually combined the alien elements of doping with carbon coating to enhance the electrochemical capability of $LiFePO_4$.

There are mainly two different doping modes, doping at the M1 site and at the M2 site. The aliovalent doping at M1 site could induce the formation of the lithium vacancy so as to ameliorate the electrochemical performance. However, in such a case, the presence of an immobile dopant at Li channel might probably block the diffusion of lithium ion [11]. Therefore, the doping at M2 site might be an ideal and promising way to

improve the electrochemical performance of $LiFePO_4$. The previous researches suggested that the replacement of Fe^{2+} by isovalent or aliovalent cation could induce the crystal lattice distortion and provide more space for intercalation/deintercalation of lithium ion. Arumugam et al. found that the specific capacity of $LiFePO_4$ was enhanced by doping 5 mol% of Mg^{2+} [12]. Yang et al. reported that the synergetic effects of V^{3+} and Al^{3+} facilitated the transport of lithium ion [13]. Jayaprakash et al. revealed that the capacity fade of $LiFePO_4$ (~1 μm) electrode material was significantly minimized and reversible capacity was increased by doping 2 mol% of Sn [15].

So far, there is no report involving the doping effects of the non-transition metal Sn on the electrochemical responses of nanocrystalline $LiFePO_4$. In this work, we firstly investigated the effects of tin-doping on microstructure and electrochemical performance of nanocrystalline $LiFePO_4$ cathode material. It was found that $LiFe_{0.97}Sn_{0.03}PO_4$ presented excellent high-rate of discharge performance and cycling stability. Therefore, $LiFe_{0.97}Sn_{0.03}PO_4$ is a promising cathode material for high-power lithium-ion batteries.

Experimental

Synthesis of precursor

The $LiFePO_4$ and $LiFe_{0.97}Sn_{0.03}PO_4$ precursors were synthesized by a simplified sol–gel approach using $FeCl_2{\cdot}4H_2O$ (Analytical Reagent (AR), 98.5%), Li_2CO_3 (AR, 99%), and H_3PO_4 (AR, >98%) as raw materials and citric acid (AR, >99.5%) as carbon source. Here, $SnCl_4{\cdot}5H_2O$ (AR, >99%) was adopted as a source of tin. The molar ratio of Li/(Fe+Sn)/P in the precursor was 1:1:1 and citric acid, in equimolar ratio to Li^+ concentration, was added. All reactants were added separately into ethanol to form the pale blue sol, maintaining magnetic stirring. After 3 h, stirring was stopped, and the gel was formed spontaneously. After drying at 358 K, the green xerogel was pre-sintered at 623 K for 5 h followed by final sintering at 923 K for 15 h in flowing Ar gas in tube furnace.

Material characterization

A Rigaku D/max 2500/PC diffractometer was used to obtain X-ray powder diffraction (XRD) patterns for the samples using Cu–Kα radiation. The diffraction data was collected at step mode over the angular range of 15~120° with a step 0.02° and a 5-s exposure time at 50 kV, 250 mA. The crystal parameters for samples were obtained by Rietveld refinement analysis using Maud program. A Pnma space group was chosen as the model. X-ray photoelectron spectroscopy (XPS, PHI 5600) equipped with a monochromatic Al (1486.6 eV) X-ray source was used to analyze the oxidation valences of Fe and Sn. The analysis of the data was performed with XPSPEAK41 processing software. All data were calibrated using adventitious C 1 s peak with a fixed value of 284.4 eV. The background from each spectrum was subtracted using a Shirley-type background. The specific surface areas of samples were measured using the multi-point (8) Brunauer-Emmett-Teller (BET) technique (Micromeritics ASAP 2020). The amount of residual carbon was determined by a chemical analysis. A certain amount of powder sample was dissolved in concentrated hydrochloride acid solution (~20 wt.%) under heating at 358 K to dissolve lithium iron phosphate. Then, the solution was filtered using the sand core funnel, and the residue was washed with dilute hydrochloride acid solution (~2.2 wt.%) and deionized water, respectively. After drying, the residual carbon was obtained. The content of remaining carbon for both samples was controlled within about 4.5 wt.%. The morphologies of samples were observed, and the average particle sizes were determined by field emission scanning electron microscopy (HITACH S4800) operating at 10 KV. Both the low- and high-resolution imaging for samples were obtained by transmission electron microscopy (TEM, JOEL JSM-2100F) with 0.17 nm point resolution and 0.14 nm line resolution. The elemental mapping was used to identify the presence and distribution of tin, phosphorus, and iron by scanning transmission electron microscopy (STEM, JOEL JSM-2100F). The electrical conductivity was measured using four-point dc methods. The sample was uniaxially pressed into pellets of 13 mm in diameter at 10 MPa, and Ag paste was coated on the both sides of the pellets.

Evaluation of electrochemical performance

The cathode electrode was prepared by mixing the as-synthesized active materials with super P and polyvinylidene fluoride at a weight ratio of 90:5:5. The CR2032 coin cell with a metallic lithium anode was assembled to evaluate the electrochemical performances of the as-obtained samples in glove-box (Mbraum, oxygen and moisture level less than 0.1 ppm). The microporous polypropylene sheet (Celgard 2500, Celgard Inc., USA) was used as the separator. One molar $LiPF_6$ solution in ethylene carbonate and diethyl carbonate (volume ratio 1:1) was used as the electrolyte. Cyclic voltammogram (CV) was carried out in the voltage range of 2.5 to 4.3 V (versus Li metal) at a scanning rate of 0.1 mV s^{-1} using VMP3 electrochemical workstation (Bio Logic Science Instruments). The galvanostatic charge/discharge cycling experiments were performed using a Land 2001A cell test system (Wuhan, China) at 298 K at different C-rates.

Results and discussion

Figure 1 shows the XRD diffraction patterns of the $LiFePO_4$ and $LiFe_{0.97}Sn_{0.03}PO_4$ samples synthesized via a simplified sol–gel approach. X-ray diffraction patterns collected in step-scan mode from two samples match with the standard fingerprint of orthorhombic $LiFePO_4$ structure (Pnma 62) very well. No crystalline metallic iron phosphides (such as Fe_2P or Fe_3P) and other crystalline substances were observed in the X-ray diffraction patterns of the Sn-doped sample. It indicates that the introduction of tin does not change the host lattice structure significantly and does not form new phases, as well. The lattice constants of the two samples have been refined by Rietveld analysis using the Maud program, and the detailed lattice parameters are listed in Table 1. It shows that the sample with Sn doping exhibits longer Li–O bond length. This shift implies that the alien element Sn has been successfully incorporated into the parent phase. In addition, STEM micrograph of the Sn-doped sample and elemental mappings of Fe, P, and Sn (shown in Fig. 2) indicate that the dopant Sn is uniformly distributed over all particles. Therefore, combined with the refinement results above, it could be concluded that the alien element Sn is evenly doped in the parent phase.

The valence states of Fe and Sn were investigated by XPS spectra. As shown in Fig. 3a, the Fe 2p core level spectra for both samples presented a typical two-peak profile and each peak is composed of a main peak and its shoulder peak. A Fe $2p_{3/2}$ main peak is at 710.6 eV with its satellite peak at 714 eV and an Fe $2p_{1/2}$ main peak is at 724.1 eV with its satellite peak at 727.4 eV. These positions correspond to the characteristic peaks of the Fe^{2+}, and the results are consistent with that reported by Dedryvère et al.

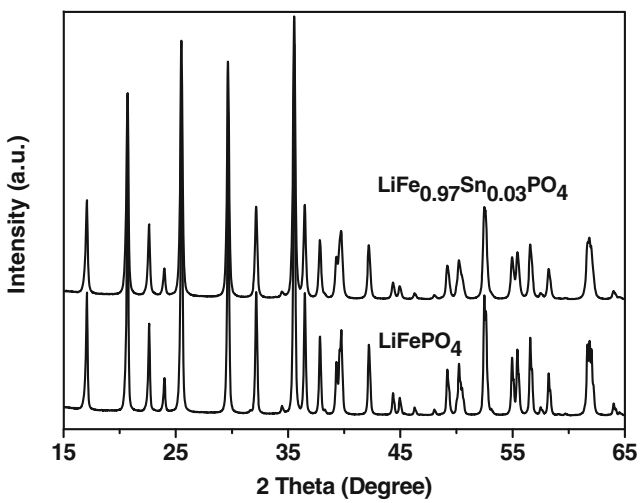

Fig. 1 XRD patterns of the as-synthesized $LiFePO_4$ and $LiFe_{0.97}Sn_{0.03}PO_4$ samples

Table 1 Lattice parameters of the original and Sn-doped samples obtained by XRD Rietveld refinements

Sample name	Original	3% Sn
Lattice constant (Å)		
a	10.32834 (5)	10.32708 (6)
b	6.00592 (5)	6.00648 (8)
c	4.69134 (8)	4.69237 (9)
Lattice volume ($Å^3$)	291.01 (0)	291.06 (6)
Interatomic distance (Å)		
$Li–O_1$	2.19411	2.19952
$Li–O_2$	1.91544	2.08904
$Li–O_3$	2.08739	2.18074
$Li–O_{mean}$	2.065 (6)	2.156 (4)
Reliability factors		
R_{wp} (%)	7.82	7.81
R_p (%)	5.47	5.59
χ^2 (%)	2.47	2.51

[16]. A pre-peak that appears at the lower binding energy side of envelope (at about 709.6 eV) is due to the formation of Fe ion with a lower valence than +2 [17]. Compared with the pristine sample, the shape of Fe 2p peaks for $LiFe_{0.97}Sn_{0.03}PO_4$ changes little. It indicates that the doping of Sn does not alter significantly the valence of Fe^{2+} cation. The Sn 3d core level spectrum for the Sn-doped sample was presented in Fig. 3b. It contains a doublet with binding energies of 486.8 and 495.5 eV, which are ascribed to the Sn $3d_{5/2}$ and Sn $3d_{3/2}$ lines, respectively. The Sn $3d_{5/2}$ line could be further fitted by two subpeaks with binding energies of 486.5 and 487.1 eV, which correspond to the Sn^{2+} and Sn^{4+} [18], respectively. The relative concentrations of Sn^{2+} and Sn^{4+} could be determined by calculating their XPS peak intensities. The intensities ratio of Sn^{2+} to Sn^{4+} is about 1.16, indicating the sample contains approximately 54% Sn^{2+} and 46% Sn^{4+}. The results imply that two different valence states of Sn cation were co-doped in the $LiFe_{0.97}Sn_{0.03}PO_4$ sample. Therefore, the mode of dopant Sn might be mixed-valence doping. Furthermore, this mixed-valence behavior could explain why the unit cell volume was almost no change after doping, as illustrated in Table 1. In this case, the cell volume is a result of the synergetic effect of mixed-valence Sn doping. The doping of larger Sn^{2+} enlarged the unit cell, just as mentioned by Jayaprakash et al. [15]; meanwhile, the doping of smaller Sn^{4+} might lead to the shrinkage of the crystal volume.

The average particle sizes of the original and doped samples were estimated based on the SEM micrographs as shown in Fig. 4a, b. Both samples consist of spherical nanoparticles and show similar morphologies. However, the

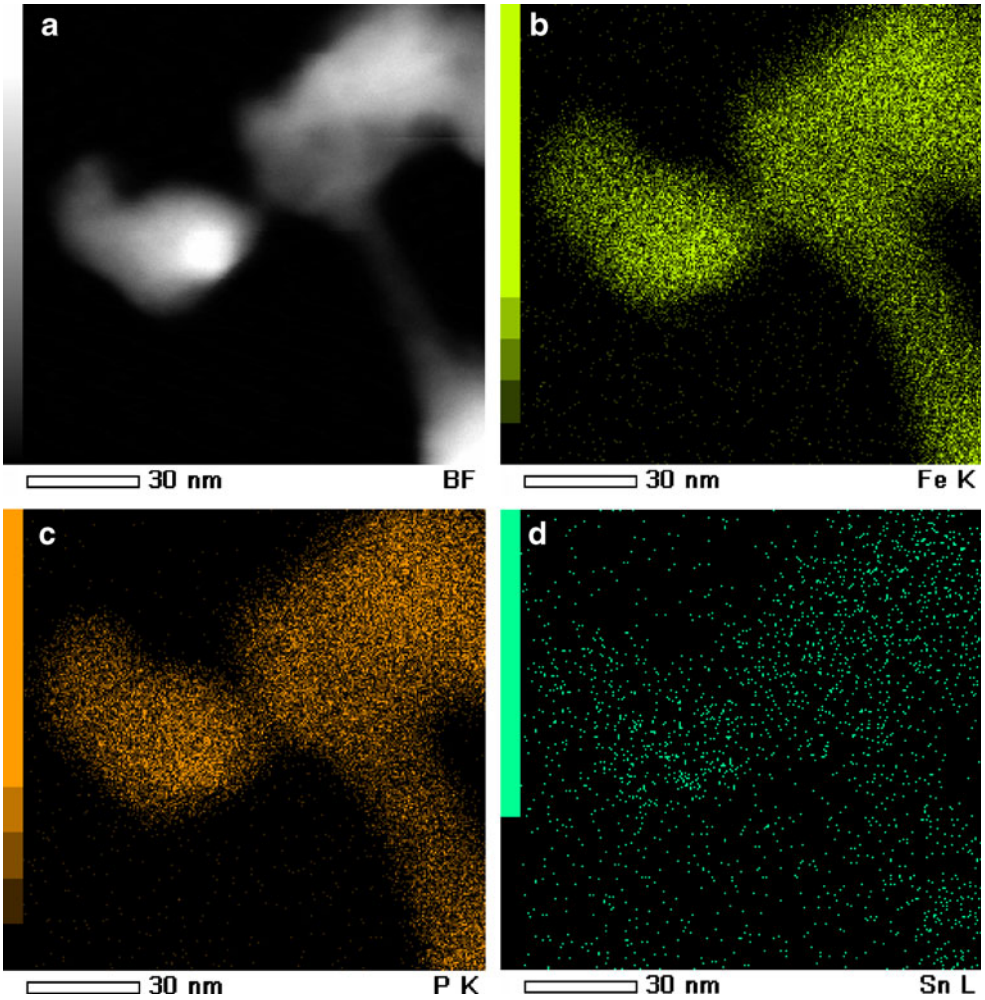

Fig. 2 STEM image and element mappings for the Sn-doped sample. **a** STEM image of the Sn-doped sample; **b** Element mapping for Fe; **c** Element mapping for P; **d** Element mapping for Sn

SEM micrographs clearly show the differences in particle size and size distribution. It is found that the average particle size is greatly reduced after doping from 71 to 60 nm, which is consistent with the increase in specific surface areas from 34.5 to 48.4 $m^2\ g^{-1}$. In addition, the doped sample shows a narrower size distribution. The relative span of the particle size distribution defined as $(D_{90}\text{-}D_{10})/D_{50}$ decreases from 0.6 to 0.4 after doping. The results indicate the doping of Sn is beneficial to obtain powder with refined particle size and uniform size distribution. The low- and high-resolution TEM images of the undoped and doped samples were displayed in Fig. 5a, b. The two samples show similar microstructure, namely an amorphous carbon layer evenly coated on the surface of the nanoparticles.

Figure 6 shows the galvanostatic discharge curves of the original and doped samples under various C-rates from 0.1 C to 10 C between 2.5 and 4.3 V. Under a 0.1 C-rate, two samples exhibit a similar specific capacity. The doped sample delivers a specific capacity of 165 mAh g^{-1}, which is similar to the $LiFePO_4$ (163 mAh g^{-1}). It indicates that the doping does not remarkably improve the specific capacity at 0.1 C. However, with increasing C-rate, the doping effect becomes more pronounced. At the discharge rate of 0.5 C, the doped sample delivers a more specific capacity of 158 mAh g^{-1}, as compared with 147 mAh g^{-1} of the pristine sample. The increase of specific capacity could be attributed to the enhanced mobility of Li^+ and high electrical conductivity. As illustrated in Table 1, the doping effect of Sn induces the lattice distortion and Li–O bond lengthening, which would facilitate Li^+ intercalation/deintercalation in the $LiFePO_4$ lattice during the charge/discharge process [13]. Moreover, the electrical conductivity of the doped sample (about 3.47×10^{-3} S cm^{-1}) is approximately one order higher than that of the pristine one (about 3.08×10^{-4} S cm^{-1}).

Under the high C-rate (≥1 C), the doped sample shows a significant improvement in the specific capacity. The doped sample delivers 154, 146, and 128 mAh g^{-1} at 1 C, 5 C, and 10 C, respectively. In contrast, the pristine one only yielded respective 134, 119, and 107 mAh g^{-1}. It is evident that the Sn doping greatly enhances the rate capability of

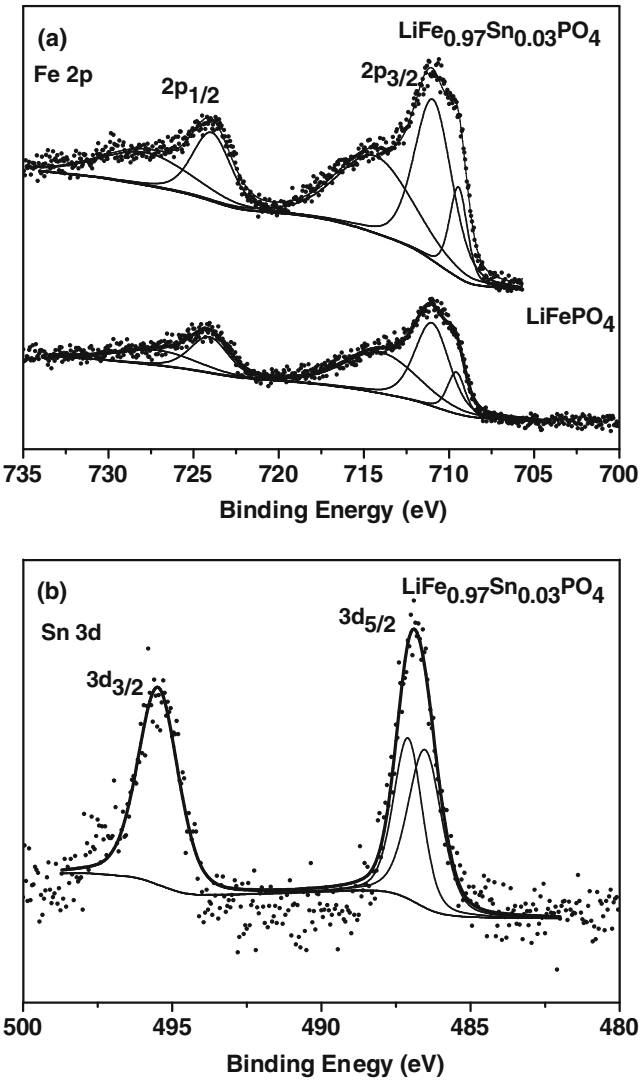

Fig. 3 Fe 2p and Sn 3d core level XPS spectra for the original and Sn-doped samples. The *solid line* represents the individual peaks and the total fit. The experimental data are presented by *dots*

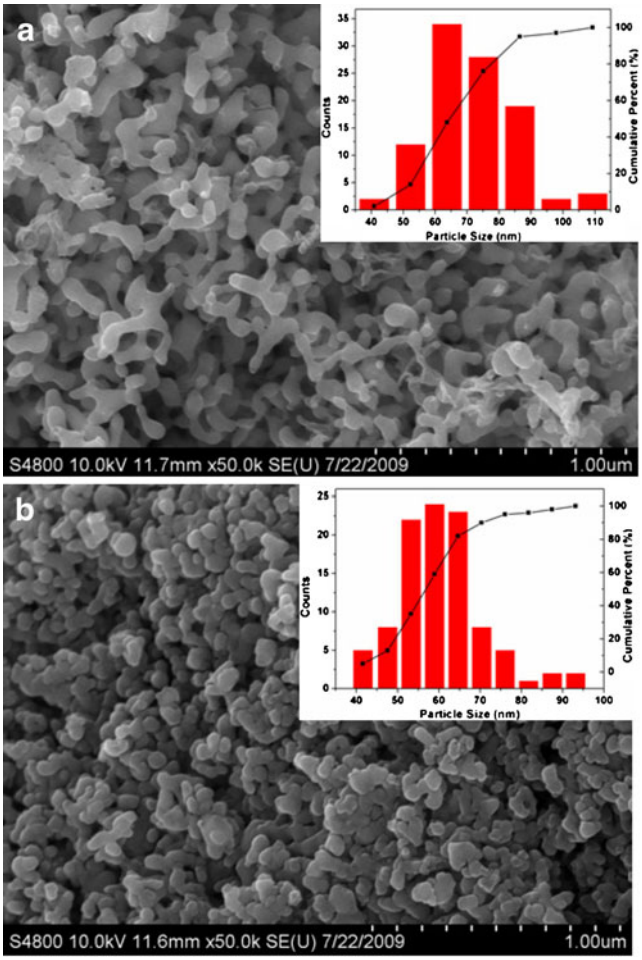

Fig. 4 SEM images of the original and Sn-doped samples. **a** The original sample; **b** The Sn-doped sample. *Inset*: particle size distributions of the pristine and Sn-doped samples

cathode material. In addition, compared with the galvanostatic discharge curves of the undoped sample, the Sn-doped sample shows a shorter flat part and a longer sloped part. And with increasing of the current density, the flat part becomes shorter meanwhile the sloped part becomes longer (shown in Fig. 6). The constant-voltage plateau indicates the two-phase electrochemical reaction between $LiFePO_4$ and $FePO_4$ while the sloped part could be considered indicative of the solid solution behavior. Yamada et al. [19] reported a narrow miscibility domain of Li_xFePO_4 and $Li_{1-y}FePO_4$, closing to the end members of $LiFePO_4$ and $FePO_4$. When the particle size of electrode materials is less than about 100 nm, this effect is more pronounced. A solid solution behavior can happen within the miscibility region. In the charge/discharge capacity curves, it is represented as a sloping profile straying from the plateau for the two-phase transition [19, 20]. Moreover, upon reducing particle size, the solid solution behavior would become much more significant [21]. Therefore, it is clear that the Sn-doped sample displays a pronounced solid solution behavior due to the nanosized effect (about 60 nm). This solid solution behavior would be beneficial to achieve the excellent electrochemical performance, especially the power capability. In order to further describe this solid solution behavior mentioned above, we calculated the surface area normalized capacitance. Under 1 C, 5 C, and 10 C, the surface area normalized capacitances are approximately 100, 126, and 188 μF cm^{-2}, respectively. These values are several times higher than the typical values of the double-layer capacitance for all electrodes, which is usually the order of 10–50 μF cm^{-1} in the aqueous electrolyte and less in nonaqueous solvents [22]. The higher surface area normalized capacitance suggests that the pseudocapacitive behavior takes place through Faradaic process involving the

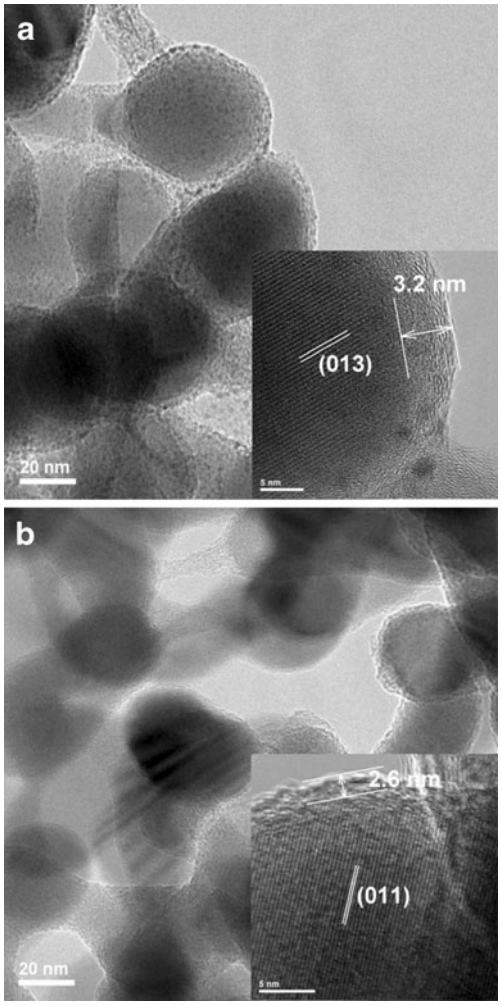

Fig. 5 TEM images for the pristine and Sn-doped samples. **a** The pristine sample; **b** The Sn-doped sample

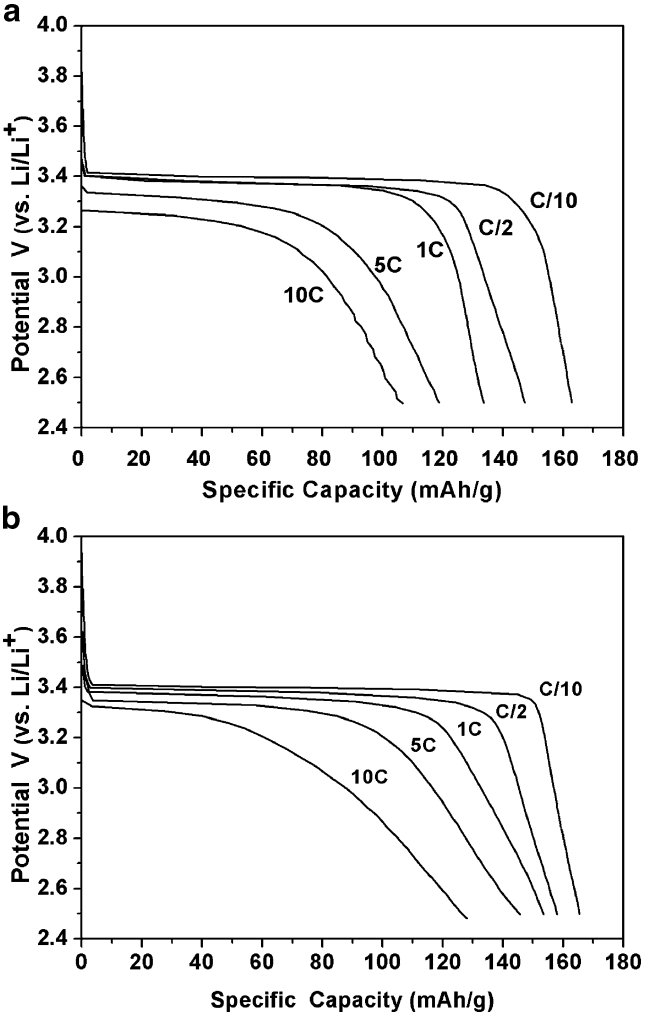

Fig. 6 The discharge curves of the original and Sn-doped samples at the different C-rates. **a** The original sample; **b** The Sn-doped sample

movement of Li^+ and electron at the surface or interface, which is coupled with the double-layer capacitance (usually much smaller). Obviously, the doped sample involved two different charge storage mechanisms, namely Li^+ electrochemical storage mechanism and the pseudocapacitive storage mechanism. This size-dependent nature of the pseudocapacitive effect has been observed in high BET surface area, nanostructured materials [23–26]. This phenomenon has been confirmed to be helpful to provide a high power density without sacrificing high energy capability and could even blur the distinction between supercapacitors and batteries [27].

In addition, under the lower C-rates, the voltage plateaus of two samples in the discharge curves have little change. However, when the C-rate is higher than or equal to 5 C, the potential drop of the undoped sample is significantly larger than that of the Sn-doped sample. It indicates that the doping decreases the Ohmic polarization resistance (R_{cc}) of electrode, which could be attributed to the enhancement of the electrical conductivity and lithium-ion velocity.

The effect of Sn doping on the $LiFePO_4$ electrode could be further clarified by CV measurement. Figure 7 shows the CV profiles of the original and Sn-doped samples. Both CV curves show one anodic peak (charge process) at about 3.5 V and one cathodic peak (discharge process) at about 3.3 V, respectively. The midpoint of the anodic and cathodic peaks for $LiFe_{0.97}Sn_{0.03}PO_4$ is about 3.43 V, in good agreement with the open-circuit voltage of the original sample. Because no additional redox peaks are found, the dopant Sn does not participate in the redox reaction. However, its peak currents are nearly twice as the original one. The enlargement of peak current should be ascribed to the increase in specific surface area and lithium-ion diffusion velocity, which is caused by Sn doping. Theoretically, we can measure the true separation between the anodic and cathodic peaks at an extremely small scan rate; however, the test instrument can only actually apply

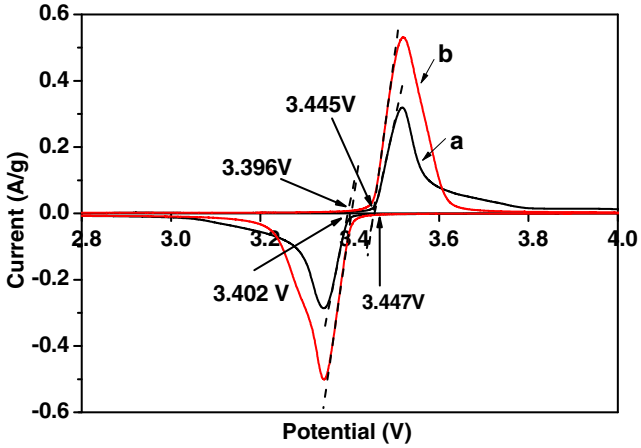

Fig. 7 The CV profiles of the original and Sn-doped samples measured at room temperature with a scanning rate of 0.1 mV s^{-1}. *a* the original sample; *b* the Sn-doped sample

the lowest scan rate of 0.01 mV s^{-1} [28]. Thus, in order to avoid this limit, we have extrapolated the envelope of the CV profiles to the *X* axis (Fig. 7) to obtain true anodic voltages of 3.447 and 3.445 V and cathodic voltages of 3.396 and 3.402 V for both samples, respectively. Because the potential difference of the doped sample (about 43 mV) is less than that of the undoped one (about 51 mV), it can be concluded that the doping enhances the reaction reversibility, which is in good agreement with results reported by others [9, 13].

The potential differences of both samples are not beyond 58 mV at 25 °C, thus the CV profiles can be analyzed using a reversible reaction model [28], in which the apparent diffusion coefficient of lithium ion could be calculated by using the peak current Eq. (1):

$$i_p = 0.4463nF\left(\frac{nF}{RT}\right)^{\frac{1}{2}} C_{Li}\nu^{\frac{1}{2}}AD_{app}^{\frac{1}{2}}K \quad (1)$$

where i_p is the oxidation peak current, n is the electron number per molecule participating in the oxidation process, F is Faraday′s constant, C_{Li} is the concentration of lithium ion, ν is the scan rate, A is specific surface area of electrode, D_{app} is apparent diffusion coefficient of lithium-ion, and K is the degree of irreversibility (0.78) [28–30]. The diffusion coefficients of lithium ion for the original and Sn-doped samples are calculated to be 6.90×10^{-11} and 2.89×10^{-10} cm^2 s^{-1}, respectively. It reveals that the doping has a positive effect on the diffusion velocity of lithium ion, which is similar to the results reported by other authors [9, 13]. The improvement of lithium-ion diffusion could be explained by the smaller particle size, narrower size distribution, and extension of Li–O bond length, which caused by the doping of Sn. Based on the shrinking core mode, the smaller particle size would effectively shorten the diffusion distance of electron and lithium ion within particles, which will be benefit to the mobility of Li^+ and thus to improve rate capability. The uniformly distributed particles with smaller size could offset the barrier to the sluggish charge transport of phosphate [31] and would increase the utilization ratio of the active materials which boosts the specific capacity. The crystal distortion induced by doping would lower the energy barrier to diffusion of lithium ion along [010] direction. The long Li–O bond distance would have a lower energy barrier and thus the lithium-ion migration could become easier. The results are consistent with the results of the electrochemical performance and microstructure.

Figure 8 shows plot of the discharge capacity vs. cycle number for the $LiFePO_4$ and $LiFe_{0.97}Sn_{0.03}PO_4$ samples under the current rate from 0.1 C to 10 C. It could be seen that the doping of Sn almost does not influence the cycling performance of $LiFePO_4$ cathode material. Even under the high discharge rate of 10 C, $LiFe_{0.97}Sn_{0.03}PO_4$ cathode also exhibits excellent cycling stability over 100 cycles. It may be attributed to the optimization of the particle size, electrical conductivity, and lithium-ion diffusion, which is induced by Sn doping.

Conclusion

Nanocrystalline $LiFePO_4$ and $LiFe_{0.97}Sn_{0.03}PO_4$ power were prepared by a simplified sol–gel synthesis. The physicochemical properties of samples were characterized using XRD, XPS, SEM, TEM, and elemental mapping. The pertinent electrochemical performances were investigated by CV and galvanostatic charge/discharge tests. The doping of Sn is beneficial to refine crystal size, increase the

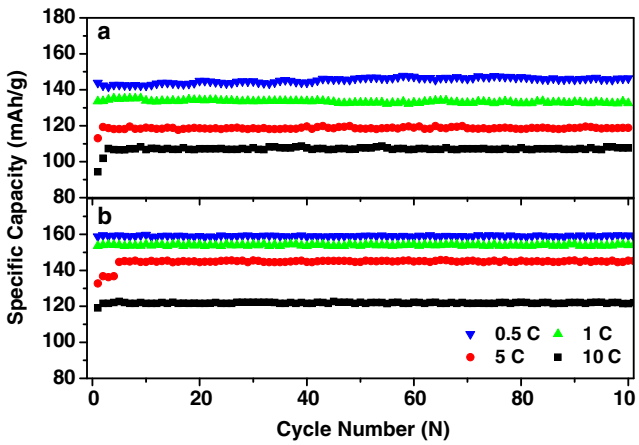

Fig. 8 Variation of discharge capacities verse cycle number for the original and Sn-doped samples cycled between 2.5 and 4.3 V at different C-rates. **a** The original sample; **b** The Sn-doped sample

electrical conductivity, and improve the mobility of Li^+. The doping plays a positive role in improving the electrochemical performance of cathode material. With the increase of C-rate, the doping effect becomes more pronounced. At 0.5 C, $LiFe_{0.97}Sn_{0.03}PO_4$ shows a specific capacity of 158 mAh g^{-1}, higher than that of $LiFePO_4$, 147 mAh g^{-1}. Under the high discharge rate of 5 C and 10 C, $LiFe_{0.97}Sn_{0.03}PO_4$ delivers specific capacity of 146 and 128 mAh g^{-1}, respectively, in comparison with 119 and 107 mAh g^{-1} for $LiFePO_4$. Furthermore, the doping does not affect the cycling capability, even at 10 C. Therefore, the doping of Sn is a promising way to optimize the rate performances of $LiFePO_4$ cathode material.

Acknowledgments We thank the financial support from National Nature Science Foundation of China under Grant (no. 50632040 and no. 50802049) and Shenzhen Technical Plan Project (no. JP200806230010A and no. SG200810150054A). We also appreciate the financial support from Guangdong Province Innovation R&D Team Plan and China Postdoctoral Science Foundation no. 20100470180.

References

1. Padhi AK, Nanjundaswarmy KS, Goodenough JB (1997) J Electorchem Soc 144:1188
2. Andersson AS, Kalska B, Häggström L, Thomas JO (2000) Solid State Ionics 130:41
3. Prosini PP, Lisi M, Zane D, Pasquali M (2002) Solid State Ionics 148:45
4. Chen JM, Hsu CH, Lin YR, Hsiao MH, Fey GTK (2008) J Power Sources 184:498
5. Choi D, Kumta PN (2007) J Power Sources 163:1064
6. Croce F, Epifand AD, Hassoun J, Deptula A, Scrosati B (2002) Electrochem Solid State Lett 5:A47
7. Sides CR, Croce F, Young VY, Martin CR, Scrosati B (2005) Electrochem Solid State Lett 8:A484
8. Ellis B, Herle PS, Rho YH, Nazar LF, Dunlap R, Perry LK, Ryan DH (2007) Faraday Discuss 134:119
9. Sun CS, Zhou Z, Xu ZG, Wang DG, Wei JP, Bian XK, Yan J (2009) J Power Sources 193:841–845
10. Yamada A, Kudo Y, Liu KY (2001) J Electrochem Soc 148: A1153
11. Ellis BL, Lee KT, Nazar LF (2010) Chem Mater 22:691
12. Arumugam D, Paruthimal Kalaignan G, Manisankar P (2009) J Solid State Electrochem 13:301–307
13. Yang MR, Ke WH (2008) J Electrochem Soc 155:A729
14. Chung SY, Bloking JT, Chiang YM (2002) Nat Mater 1:123
15. Jayaprakash N, Kalaiselvi N, Periasamy P (2008) Int J Electrochem Sci 3:476
16. Dedryvère R, Maccario M, Croguennec L, Le Cras F, Delmas C, Gonbeau D (2008) Chem Mater 20:7164
17. Grosvenor AP, Kobe BA, Biesinger MC, Mclntyre NS (2004) Surf Interface Anal 36:1564
18. Song J, Cai MZ, Dong QF, Zheng MS, Wu QH, Wu ST (2009) Electrochem Acta 54:2748
19. Yamada A, Koizumi H, Sonoyama N, Kanno R (2005) Solid State Lett 8:A409
20. Delmas C, Maccario M, Croguennec L, Le Cras F, Weill F (2008) Nat Mater 7:665
21. Meethong N, Huang HYS, Carter WC, Chiang YM (2007) Electrochem Solid State Lett 10:A134
22. Conway BE, Birss V, Wojtowicz J (1997) J Power Sources 66:1
23. Wang J, Polleux J, Lim J, Dunn B (2007) J Phys Chem C 111:14925
24. Zhang H, Li GR, An LP, Yan TY, Gao XP, Zhu HY (2007) J Phys Chem C 111:6143
25. Luo JY, Wang YG, Xiong HM, Xia YY (2007) Chem Mater 19:4791
26. Kang B, Ceder G (2009) Nature 458:190–193
27. Maier J (2005) Nat Mater 4:805
28. Yu DYW, Fietzek C, Weydanz W, Donoue K, Inoue T, Kurokawa H, Fujitani S (2007) J Electrochem Soc 154:A253
29. Bard AJ, Faulkner LR (2001) Electrochemical Methods. 2nd ed. New York, Wiley. 231
30. Takahashi M, Tobishima S, Takei K, Sakurai Y (2002) Solid State Ionics 148:283
31. Yamada A, Chung SC, Hinokuma K (2001) J Electrochem Soc 148:A224